ISET Journal of Earthquake Technology, Paper No. 596, Vol. 62, No. 2, June 2025, pp. 95-111

EFFECT OF REPEATED CYCLIC STRAINING ON DYNAMIC PROPERTIES OF SILTS FROM ELEMENTAL AND *IN-SITU* TESTS

Amalesh Jana*
Assistant Professor, Montana State University
Bozeman, MT 59717, USA, Email id: Amalesh.jana@montana.edu

Ali Dadashiserej
Geotechnical Engineer, Jacobs Engineering Group
Portland, OR, USA, Email id: Ali.Dadashiserej@jacobs.com

Armin W. Stuedlein
Professor, Oregon State University, Corvallis
OR 97331, USA, Email id: Armin.Stuedlein@oregonstate.edu

T. Matthew Evans
Professor, Oregon State University, Corvallis
OR 97331, USA, Email id: Matt.evans@oregonstate.edu

ABSTRACT

This paper presents the design and execution of an *in-situ* dynamic test program evaluating the effect of strain history on the in-situ dynamic response of plastic silt deposits employing mobile shaker and controlled blasting techniques. In order to obtain the elemental viewpoint, first a series of staged, constant-volume stress-controlled, and strain-controlled cyclic direct simple shear tests were performed on both intact and reconstituted plastic silts to examine the evolution of cyclic resistance resulting from repeated dynamic loading events. The influence of governing parameters, including post-cyclic densification, soil fabric, shear strain magnitude, potential bias in shear strain accumulation, and selection of failure criterion on the development of cyclic resistance in silts has been examined. The full-scale, in-situ dynamic testing program characterizes and compares three-dimensional dynamic response of a plastic silt deposit to multi-directional loading. Changes in soil fabric were quantified using small-strain shear wave velocity measurements performed before and after each stage of dynamic testing and were linked to the observed increase and decrease in threshold shear strain to trigger excess pore pressure development in soil. Findings from this study may elucidate potential implications for evaluating the effects of aftershocks following a mainshock earthquake event.

KEYWORDS: Cyclic and Dynamic Properties of Soil, Strain History, Liquefaction, In-Situ Testing

INTRODUCTION

The influence of pre-shaking on the cyclic resistance of natural soil deposits during future earthquakes remains a significant issue for practitioners and academics, particularly with mainshock-aftershock and multi-mainshock earthquake sequences. The Canterbury Earthquake Sequence exemplifies the repercussions of such events (Cubrinovski et al. 2011; van Ballegooy et al. 2014); nonetheless, the influence of strain history on the seismic behavior of soils was recognized approximately forty years ago. Post-earthquake observations indicate that successive seismic events may or may not enhance the cyclic resistance of a soil deposit in subsequent occurrences. Kuribayashi and Tatsuoka (1975) documented a sand deposit that underwent re-liquefaction during four consecutive earthquakes in northeast Tokyo, Japan, between 1894 and 1931. The natural pre-shaken silty sand deposit at the Wildlife Site in Imperial Valley, California, demonstrated increased liquefaction resistance during shaking episodes following the original liquefaction occurrence (Youd and Bennett 1983; Holzer and Youd 2007; El-Sekelly et al. 2016). Studies indicate that a single pre-shearing occurrence might either enhance or diminish cyclic resistance for subsequent events, depending on the amount of shear strain, γ, and number of loading cycles, N (Finn et al. 1970; Lee and Albaisa 1974; Ishihara and Okada 1978). Finn et al. (1970) observed that a single amplitude

https://doi.org/10.63898/IKBN3999
*Corresponding Author

threshold shear strain existed (i.e., γ_{SA} = 0.5%) for sand specimens within which pre-shearing enhances cyclic resistance by augmenting particle interlocking and eliminating local instabilities at grain-to-grain contacts. Nonetheless, substantial pre-shaking led to a significant decline in resistance and increased excess pore pressures during subsequent shaking events, attributable to the development of microstructural anisotropy, fabric rearrangement, and the degradation of soil fabric formed through aging, cementation, and biogeochemical processes, alongside corresponding decrease in initial lateral stresses (Finn et al. 1970; Oda et al. 2001; Olson et al. 2001; Wahyudi et al. 2016). Unlike the impact of a single pre-shaking event, sand deposits exposed to numerous shaking episodes may demonstrate a cumulative enhancement in cyclic resistance over geological time (Hayati and Andrus 2009; El-Sekelly et al. 2016;). Previous research has concentrated on clean or silty sand, with limited laboratory studies and case histories available for nonplastic and low plasticity silts (Price et al. 2017; Soysa and Wijewickreme 2019; Wijewickreme et al. 2019b), and even fewer for intact silts (Sanin 2005). Furthermore, there are no direct quantitative observations regarding the impacts of preshaking on threshold shear strain and the rate of excess pore pressure development *in-situ*, where preshaking could significantly influence *in-situ* pore pressure generation (Dobry and Abdoun, 2015b; El-Sekelly et al., 2016). First this study explores strain history effect on cyclic response of medium and high plastic silt deposit evaluated using cyclic direct simple shear test. Then this study describes the planning and execution of an *in-situ* dynamic test sequence using mobile shaking and controlled blasting testing techniques to quantify the effect of preshaking on the *in-situ* dynamic response of plastic silt deposits with plasticity ranging from low to high.

ELEMENTAL RESPONSE OF STRAIN HISTORY EFFECT ON CYCLIC STRENGTH OF LOW AND HIGH PLASTICITY SILT

A systematic laboratory testing program was executed on both intact and reconstituted specimens derived from high-quality thin-walled tube samples obtained from two test sites. Site B refers to the Van Buren Bridge over the Willamette River in Corvallis, Oregon (Dadashiserej et al. 2022; Stuedlein et al. 2023). Site D is situated at the Port of Portland in Portland, Oregon, as detailed by Jana and Stuedlein (2021a; 2022). Reconstituted specimens were created using the slurry-deposition technique by hydrating crushed oven-dried soil at a water content, *w*, of twice the liquid limit for a minimum of 24 hours, adhering to the procedures outlined by Soysa (2015) to generate uniform specimens that replicate the soil fabric of fluvial depositional environments (Wijewickreme et al. 2019a; Krage et al. 2020). Summary of soil properties of two different sites are presented in Table 1.

The influence of strain history and magnitude on the cyclic resistance of intact and reconstituted specimens from Sites B and D was investigated using constant-volume, staged, stress-controlled cycle tests with 0.1 Hz loading frequency. To identify the associated effects of densification arising from post-cyclic reconsolidation and fabric destruction, the specimens were subjected to similar cyclic stress ratio, *CSR* in sequential shearing stages. Figures 1a depict schematics that illustrate the staged loading methods for the stress-controlled cyclic direct simple shear, CDSS tests, which encompass several cyclic loading and reconsolidation phases. Upon the end of primary consolidation, the cyclic loading phase commenced under a designated *CSR*. After the cyclic loading phase ended, the specimens were recentered in the direct simple shear, DSS device and reconsolidated to the initial vertical effective stress, σ'_{vc} in preparation for the subsequent cyclic phase. The subsequent cyclic phase began after the dissipation of excess pore pressures and the measurement of small strain shear wave velocity, V_s using a bender element system fabricated within the top and bottom platen of the *CDSS* apparatus (Dadashiserej 2022).

Table 1: Summary of soil properties of two sites

Soil Properties	Site B	Site D
Soil Type	Low-plasticity silt, ML	High-plasticity silt, MH
Natural water content, w_n	41% to 59%	75%
Plasticity index, *PI*	13 to 15	26%
Fines content, *FC*	86% to 94%	100%
Clay Fraction (<2μ)	N/A	16%
Overconsolidation ratios, *OCR*	1.7	1.9

Several constant-volume, staged, strain-controlled, cyclic tests with shear wave velocity measurement were carried out with 0.1 Hz loading frequency on reconstituted normally consolidated, *NC* and overconsolidated, *OC* specimens from Site D. This was done because stress-controlled cyclic tests were unable to capture the effect of soil fabric due to the application of medium to large strains in the first cycle of loading and biased accumulation of shear strain during stress-controlled conditions. These strain-controlled studies were designed to capture the effects of a wide variety of shear strain magnitudes and soil fabric on the cyclic response. Figures 1b depict two loading protocols for the constant-volume, staged, strain-controlled cyclic testing, comprising three identical and repeated loading sequences at four different shear strain amplitudes, resulting in a total of twelve unique stages. Each series comprises the number of loading cycles, $N = 30$, at four consistent amplitudes of shear strain. Specimens underwent a reconsolidation phase after each cyclic shearing phase. The maximum shear strain amplitude in a series is associated with the final cyclic shear stage, where shear strain = 1% is denoted as small shaking (denoted T1) and 3% as strong shaking (denoted T2).

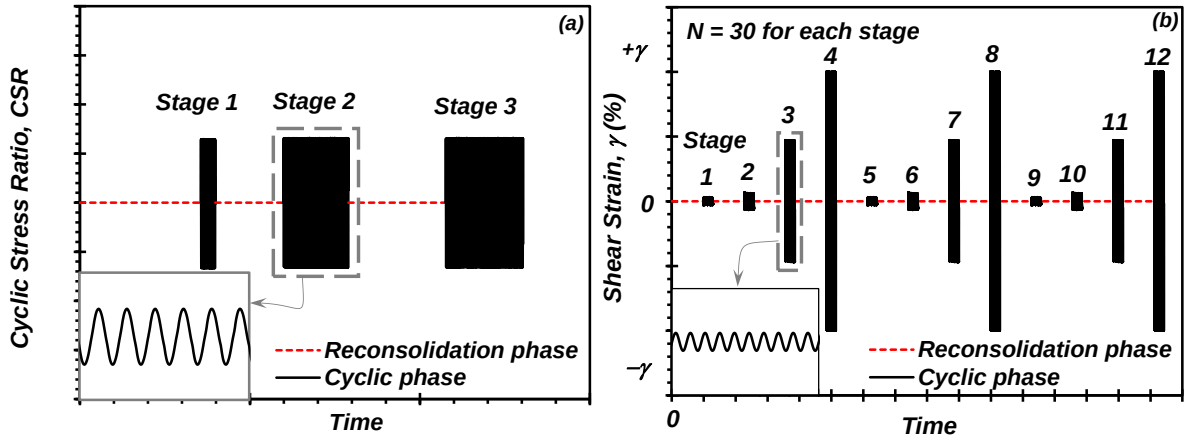

Fig. 1 Loading protocols for staged cyclic DSS tests: (a) stress-controlled loading and (b) strain-controlled loading (modified after Dadashiserej et al. 2022)

Figure 2 illustrates instances of multiple shearing stages for the Site B intact specimen BU1, depicting the normalized shear stress-shear strain, *CSR*-γ, hysteresis throughout three cyclic loading stages. After reconsolidation at σ'_{vc} = 160 kPa, specimen BU1 was initially subjected to a *CSR* of 0.26 (BU1-S1), which was terminated at a maximum shear strain of γ_{max} = 8.5% after N = 25.5, followed by reconsolidation and

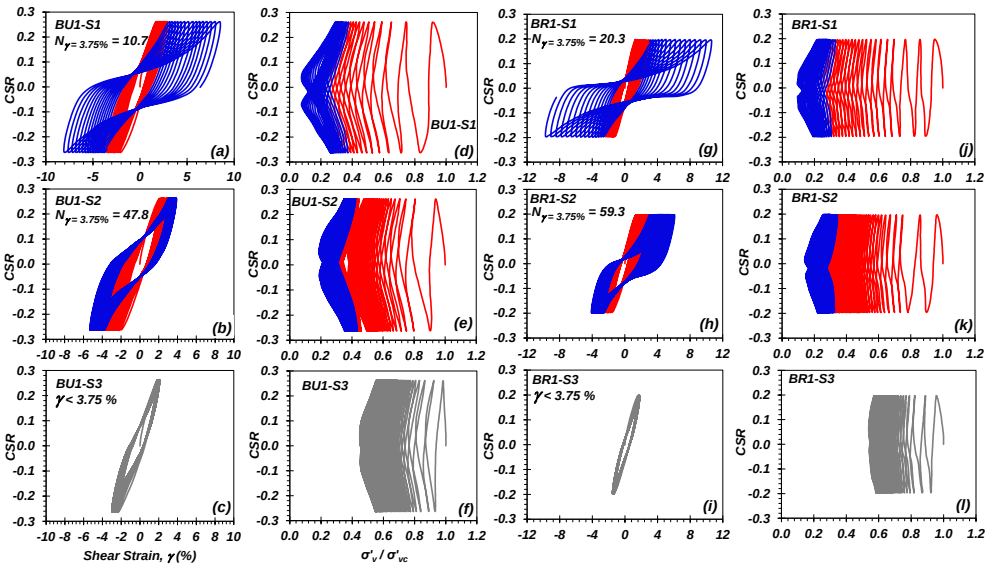

Fig. 2 Staged constant-volume, stress-controlled CDSS results of intact (BU1) and reconstituted specimen (BR1) from Site B: (a, b, c, g, h and i) stress strain hysteresis, and (d, e, f, j, k and l) effective stress paths (modified after Dadashiserej et al. 2022)

shearing in succeeding phases (i.e., BU1-S2 and BU1-S3). Figures 2a – 2c depict the *CSR*-γ hysteresis for BU1-S1, BU1-S2, and BU1-S3, respectively, showcasing a gradual improvement in cyclic resistance at each loading step, yielding a number of cycles to reach single amplitude shear strain of 3.75%, $N_{\gamma SA=3.75\%}$ values of 10.7, 47.8, and $N_{\gamma SA=3.75\%}$ >136. It is seen that at a fixed *CSR*, $N_{\gamma SA=3\%}$ and $N_{\gamma SA=3.75\%}$ increase significantly ($N > 100$) after reconsolidation and densification. The effective stress path of the same loading stages (Figures 2d to 2f) indicates a dilative tendency for the subsequent dynamic loading sequences and lower excess pore pressure development. The decrease in the specimen's void ratio, e_c, due to post-cycle volumetric strain, ε_{vpc}, during subsequent reconsolidation contributes to the improvement of cyclic resistance. The decrease in e_c outweighed the adverse impacts linked to the degradation of soil structure resulting from the previous strain history, with γ_{max} of 8.5, 5.3, and 3% for BU1-S1, BU1-S2, and BU1-S3, respectively. A similar response was observed in case of reconstituted specimens from Site B (BR1) as shown in the Figure 2. Due to brevity, CDSS results for other specimens are not discussed here and can be found in Dadashiserej et al. (2022).

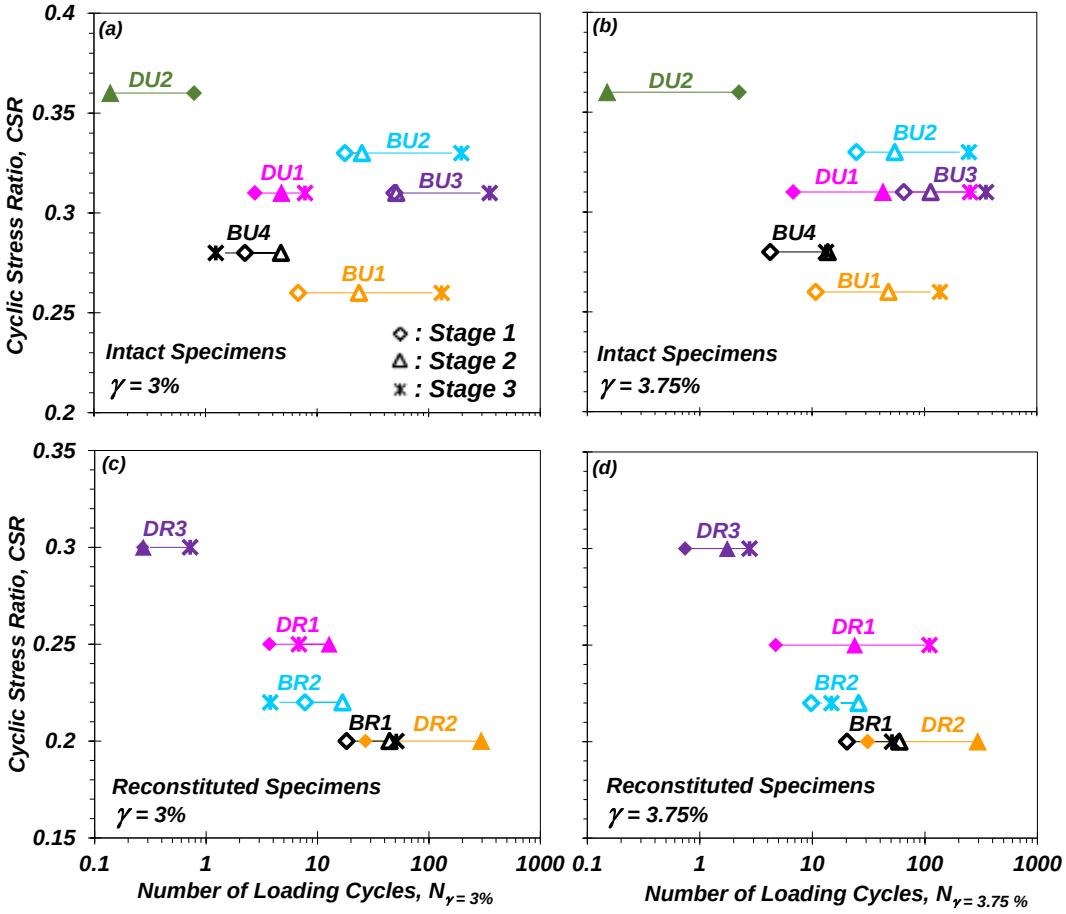

Fig. 3 Effect of staged cyclic loading on cyclic resistance for intact and reconstituted specimens from Site B and D evaluated based on shear strain failure criterion: (a and c) γ_{SA} = 3%, and (b and d) γ_{SA} = 3.75% (modified after Dadashiserej et al. 2022)

The variation of *CSR* with $N_{\gamma SA=3\%}$ and $N_{\gamma SA=3.75\%}$ for both intact and reconstituted specimens from Sites B and D are shown in Figure 3 to highlight how the choice of cyclic failure threshold can affect the interpretation of pre-straining. Reconstituted specimens BR1 and BR3 demonstrated progressive increases in $N_{\gamma SA=3.75\%}$, in contrast to the inconsistent variations in cyclic resistance observed with $N_{\gamma SA=3\%}$. This discrepancy arises because, during the latter stages of loading, the increased dilative tendency diminishes the rate of shear strain accumulation per cycle due to post-cyclic densification. Consequently, the number of cycles required to achieve a specific γ is significantly influenced by the magnitude of γ during the initial loading cycle. The cyclic resistance of the specimen is highly sensitive to the selection of the shear strain failure criterion (Price et al. 2017). The application of a strain-based cyclic failure criterion is advantageous for evaluating cyclic resistance in the simplified method (e.g., Idriss and Boulanger 2008) for cyclic

softening assessments; however, there is no fundamental rationale for the choice of an arbitrary strain amplitude (Wijewickreme and Soysa 2016). The findings of this study clearly demonstrate the influence of using a strain-based failure criterion on the evaluation of the cyclic resistance of soil under repeated cyclic loading.

Several constant-volume, staged, strain-controlled, cyclic tests with shear wave velocity measurement were carried out to capture the effect of strain history on soil fabric. The staged, cyclic response of the *NC* and *OC (OCR = 2)* specimens to small (TS; Figure 4a) and large (TL; Figure 4b) shakings is shown in Figure 4. According to Dobry et al. (1982) and Hsu and Vucetic (2006), the excess pore pressure ratio at the end of each cycle is known as the residual excess pore pressure ratio, or $r_{u,r} = \Delta u_r / \sigma'_{vc,}$ where Δu_r is residual excess pore pressure. The difference in $r_{u,r}$ between *NC* and *OC* specimens under TS loading showed that, for both smaller (S1, 2, 3, 5, 6, 7, 9, 10, and 11) and larger shear strain magnitudes (S4, 8, and 12), $r_{u,r}$ gradually declined between the first and last stages. For instance, over consolidated specimen subjected to small shaking, OC-TS demonstrated a decrease in $r_{u,r}$ from 8.5% at S4 to 5.3% and 3.9% in stage S8 and S12 when subjected to a constant γ_{SA} = 1% in S4, 8, and 12, respectively. The improvement in cycle resistance as indicated by the 54% reduction in $r_{u,r}$ from S4 to S12 for is clearly evident despite a near-constant void ratio (Figure 4e) and the slight rise in V_s (i.e., 0.1%; Figure 4f). Conversely, the densification of normally consolidated specimen subjected to small shaking, NC-TS results in a slight increase in cyclic resistance, as evidenced by the observed change in void ratio from e = 1.07 to 1.04.

It is possible to find comparable patterns in responses for stages that have lower amplitudes of shear strain. Despite the small shaking not causing substantial alterations in density, a stronger soil fabric was established, as evidenced by the variation in V_s. This development is presumed to have occurred through the elimination of local instabilities, enhancing of lateral stresses, and reorganization of soil particles (Finn et al. 1970; El-Sekelly et al. 2017), aligning with the influence of pre-shaking on a young, reconstituted silty sand noted by El-Sekelly et al. (2016). Figure 4d depicts the impact of significant shaking (i.e., TL loading) on the formation of $r_{u,r}$ in *NC* and *OC* specimens.

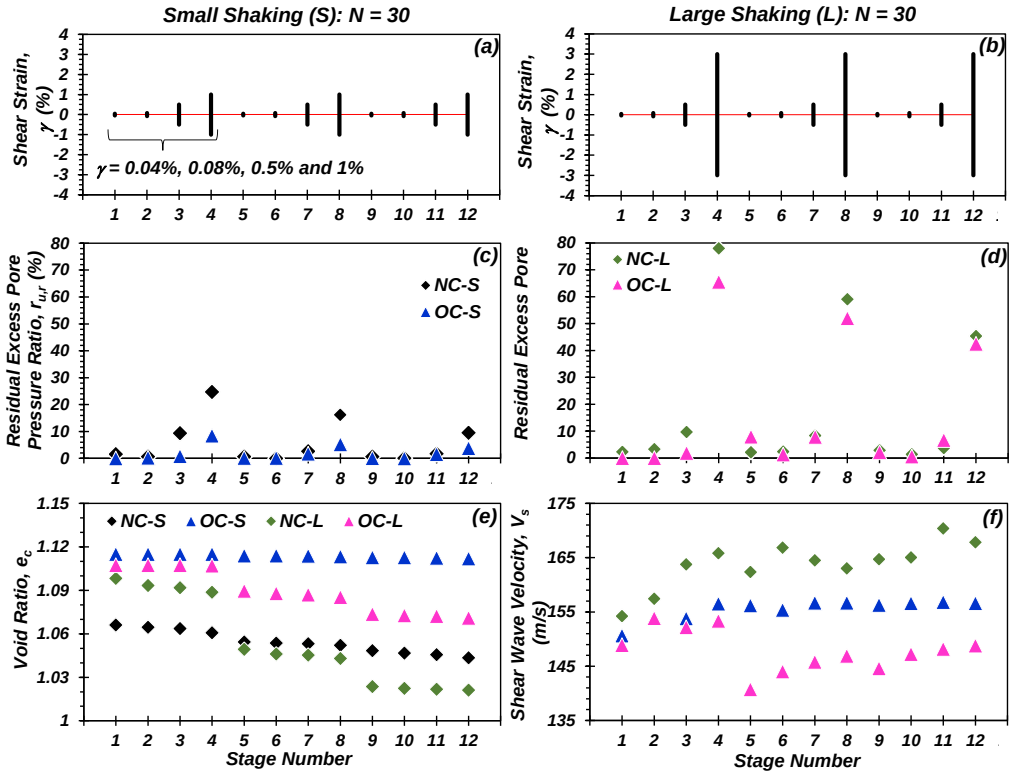

Fig. 4 Summary of staged constant-volume, strain controlled CDSS tests on reconstituted normally consolidated (*NC*) and overconsolidated (*OC*) specimens: loading protocol for (a) mild shaking and (b) large shaking; variation of residual excess pore pressure response for (c) mild shaking and (d) large shaking; strain history effect on *NC* and *OC* specimens due to mild and large shaking showing: (e) variation of void ratio, and (f) shear wave velocity (modified after Dadashiserej et al. 2022)

Similar to specimens OC-TS and NC-TS, specimen NC-TL showed a decrease in $r_{u,r}$ for stages with larger (S1, 2, 3, 5, 6, 7, 9, 10, and 11) and smaller magnitudes of shear strain. The NC-TL specimen's cyclic behavior and pore pressure response were controlled by post-cyclic densification, which produced a more dilative response even though the S4 loading with γ_{SA} = 3% may have destroyed the soil fabric and partially or completely eliminated the beneficial effect of earlier low amplitude cyclic shear strains during stages S1 through S3. The cyclic behavior of specimens OC-TL and NC-TL was markedly different from one another. Following S4 loading with a substantial shear strain magnitude (γ_{SA} = 3%), specimen OC-TL exhibited larger $r_{u,r}$ in subsequent smaller amplitude loading stages (i.e., S5, 6, 7, 9, 10, and 11). The increased generation of excess pore pressure occurred despite the reduction in void ratio over S1 to S4 (i.e., from e_c = 1.11 to 1.09; Figure 4e). The rise in $r_{u,r}$ that was observed suggests that S4 caused some damage of the fabric, eliminated any potential advantages of low amplitude cyclic straining, and decreased lateral stresses. These observations are fully consistent with the changes observed in V_s (Figure 4f).

In summary, *NC* and *OC* specimens that underwent mild shaking demonstrated a consistent pattern in reducing the buildup of excess pore pressure during cyclic phases. During strong shaking, stress history critically influences the $r_{u,r}$-based cycle resistance following the initial large strain magnitude phase, potentially leading to a considerable adverse change in the soil fabric of overconsolidated specimens and their associated cyclic resistance. During the subsequent phases of intense shaking, the *OC* specimen regained a portion of its resistance and experienced a comparable decrease in the generation of excess pore pressure as the *NC* specimen (Figure 4f). In comparison, the variation of shear wave velocity with stage in specimens OC-TS, NC-TL, and OC-TL (Figure 4f) indicates that shear wave velocity is more responsive to modifications in stress state and soil fabric than to changes in density (Figure 4e).

This element testing program highlighted the importance of strain history on silty soils. However, there are no direct quantitative measurements concerning the effects of preshaking on threshold shear strain and the rate of pore pressure development *in-situ*, where preshaking may substantially affect *in-situ* pore pressure generation. The development and execution of a novel *in-situ* dynamic test program employing mobile shaking and controlled blasting techniques to assess the impact of preshaking on the *in-situ* dynamic response of low to high plastic silt deposits is described below.

VIBROSEIS SHAKING AND CONTROLLED BLASTING OF A LOW PLASTICITY SILT DEPOSIT

1. Test Site Characterization and *In-Situ* Dynamic Test Program

The low-plasticity test site is located at the Port of Longview, Washington, USA. The underlying stratigraphy of the experimental array comprises dense silty sand with gravel fill to a depth of 0.4 m, underlain by a deposit of medium stiff sandy silt (ML) transitioning to soft clayey silt to silty clay (ML to CL) extending to roughly 1 m. This layer was underlain by a 1.2 m thick deposit of very soft to soft, clayey silt to silty clay (MH to CH), succeeded by an approximately 0.6 m thick layer of soft to medium stiff clayey silt (ML), mixed with occasional stringers of sandy silt. A substantial layer of soft, clayey silt extending to the depth of the investigations was noted, and adjacent explorations indicate that the underlying basalt bedrock may be found at depths ranging from 60 to 80 meters below the surface. The groundwater table depth below the surface, as measured during cone penetration test, CPT, soundings and pore pressure transducers was 1.45 m. The groundwater table's depth varied annually due to its proximity to the Columbia River, located approximately 1 km south of the site.

The general concept for this instrumented dynamic test program is to observe the soil responses to body waves triggered by a vibroseis truck and controlled blasting. The goal is to monitor particle velocities at the "nodes" comprising "finite elements" formed by the geometry of the placed triaxial geophone packages, TGPs and the use of numerical methods developed for finite element analyses (FEA) to determine the strains developed within the array. Each TGP consists of three geophones arranged in mutually perpendicular directions to measure particle velocity in the three orthogonal directions of interest, and one dual axis Micro-electromechanical systems, MEMS accelerometer to measure the as-installed static tilt angle of each package in two orthogonal directions. Forty-two individual geophones were used to fabricate fourteen triaxial geophone packages (TGPs). Pore pressure transducers, PPTs placed in the center of the elements provide the excess pore pressure response to the strains imposed at the mid-point of each finite element to complete the instrument array, termed the Silt Array.

The geometry of the sensor array implanted at the test site was designed to formulate two *in-situ* solid (3D) elements at different depths to compute the three-dimensional strain tensor from the dynamic loading applied by the Natural Hazards Engineering Research Infrastructure at the University of Texas at Austin vibriosis, NHERI@UTEXAS T-Rex mobile shaker (Stokoe et al. 2017) and the controlled blasting event. Because near-field blast pulses produce three-dimensional body waves, the solid element formulation was thought to provide a more accurate estimate of shear strains for charges located close to the array. The schematic three-dimensional view, top view, side elevation view facing west, and the front elevation view facing north is shown in Figure 5. Fourteen TGPs and three PPTs were used to formulate the two solid elements at different depths of the soil strata. The geometry of the sensor array was optimized in view of competing factors: the soil inside the array must experience as little disturbance as possible, and the sensors should be as close to one another as possible and dictated by the wavelength of the body waves to be observed. The maximum distance between the sensors should be one quarter of the wavelength as described in Cox (2006). The geometry deployed was selected in consideration of the *in-situ* V_s and anticipated predominant frequency of the blast-induced S-waves.

Following the installation of each sensor in the ground, three sets of experiments were conducted: (1) shaking with T-Rex, (2) controlled blasting, and (3) downhole testing conducted immediately before and after shaking and blasting. Given the comparatively low-to-moderate strain magnitudes exerted by T-Rex, shaking was conducted prior to the controlled blasting experiment. The T-Rex base plate was aligned with Element 2 (formed by TGP S1, S2, S3, S4, S5, and S6), but a portion of Element 1(formed by TGP S9, S10, S11, S12, S13, and S14) extended beyond the front edge of the base plate (Jana et al. 2023). A third tetrahedral array, Element 3 (formed by TGPs S10, S9, S11, and S7), was also analyzed for comparison with measurements made using PPT-2. The vertical force exerted on the baseplate was approximately 200 kN. After positioning the mobile shaker above the sensor array and allowing the excess pore pressures induced by the truck's weight to dissipate, mobile shaking at different amplitudes began. Uniaxial shaking was conducted in the east-west direction, aligned with the blast casings as detailed below, to generate maximum velocity amplitudes along the "x" (east-west) component of each TGP (Figure 6a). Five shaking events (Stages 1 through 5) were executed with uniaxial sinusoidal motion applied for 4 seconds at a loading frequency of 10 Hz, with each loading phase succeeded by the dissipation of excess pore pressure produced in the preceding loading phase (Figure 6b).

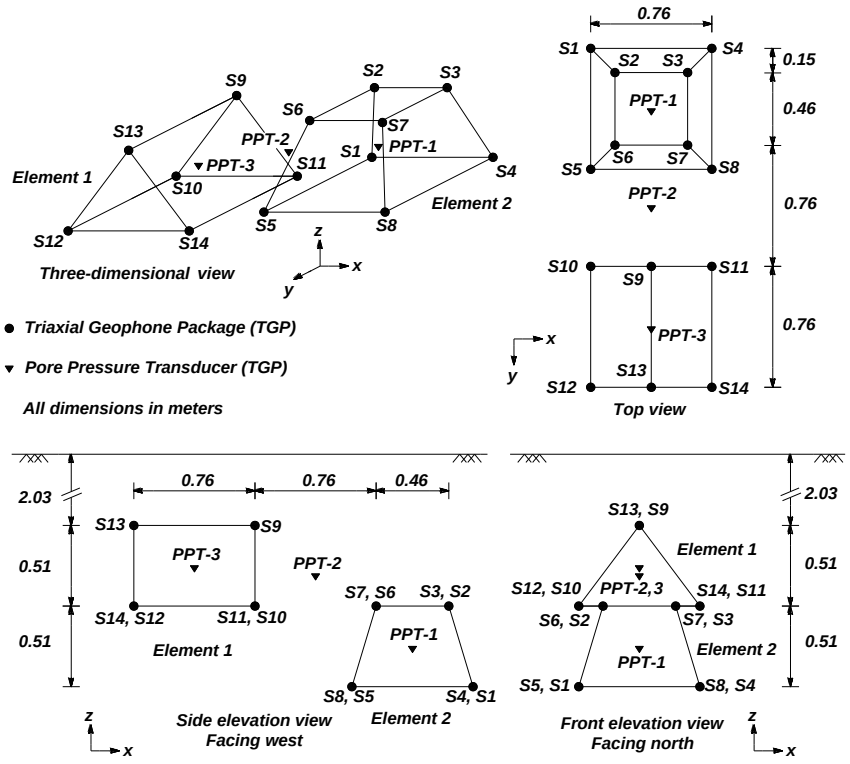

Fig. 5 Schematic of the Silt Array used at the Port of Longview consisting of TGPs and PPTs to formulate two 3D finite elements in-situ: (a) schematic 3D view, (b) top view, (c) side elevation view facing west, and (d) front elevation view facing north (modified after Jana 2021)

The experimental setup for the controlled blasting experiment conducted at the Port of Longview is shown in Figure 6. Twelve blast casings were installed: casings CX1 and CX2, which were positioned north of the array and equipped with small charges to probe the Silt Array and measure the small-strain shear wave velocity between the detonations of larger charges, whereas the remaining ten were positioned east-west to provide a primarily 2D waveform towards the instrumented array. The blast casings were positioned 0.92 m apart from the east-west alignment to reduce potential interference with the seismic waveforms. This meant that a clear and unhindered waveform was present for every assumed linear ray path. The charge magnitude, location, and time of detonation are shown in Figure 6c, which illustrates the 30-second detonation sequence produced by 45 explosive charges. Figure 6d illustrates the elevation view of the charge positions within the ground. The experiment was designed to produce an initial linear elastic soil response and began with small charges (90 grams) placed approximately 15 m from the sensor array. As the experiment advanced, the charge weight increased as the distance to the array reduced triggering a nonlinear-elastic response followed by a nonlinear-inelastic soil reaction. Subsequent to the detonation of charges weighing a maximum of 1.36 kg, the charge weights were reduced to preserve the integrity of the TGPs.

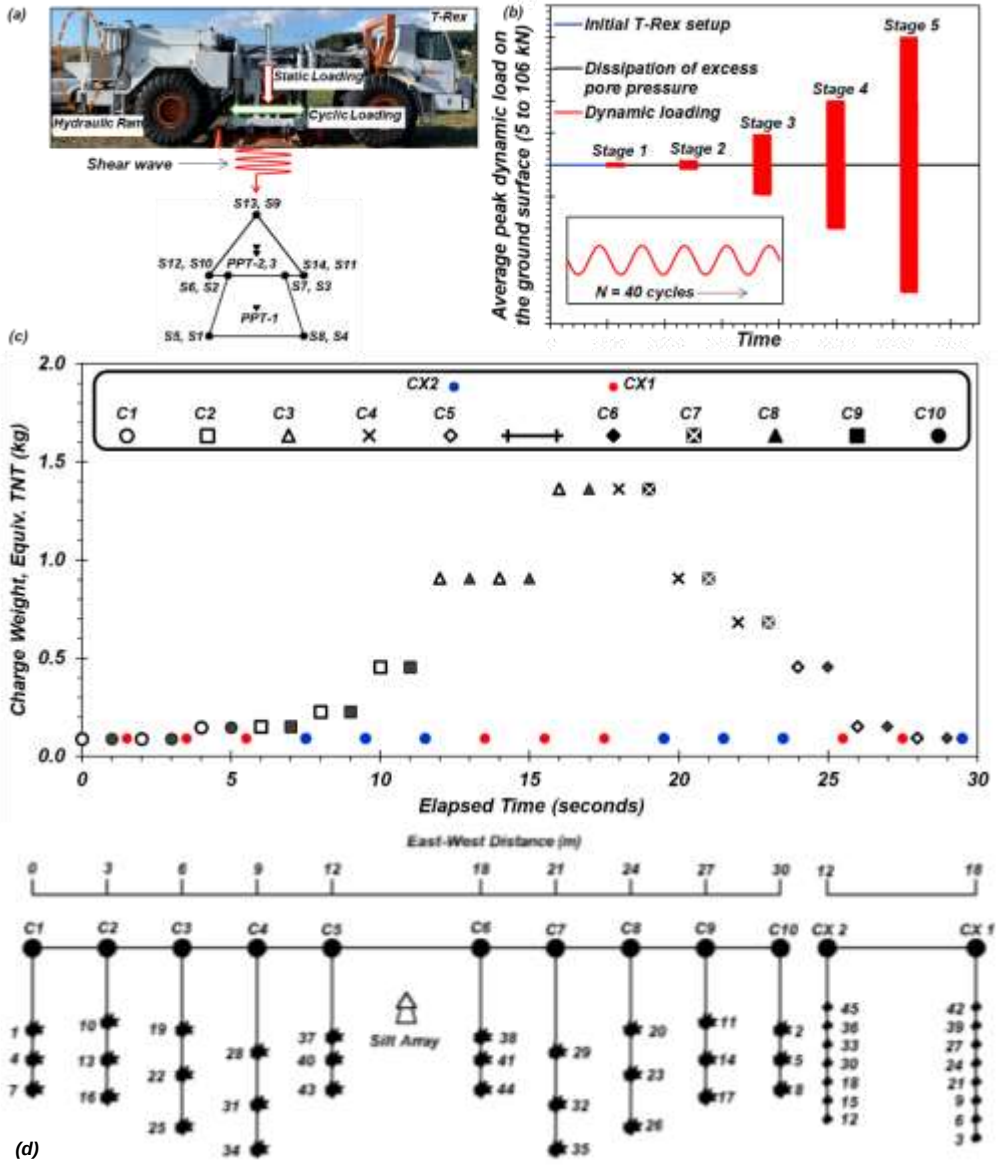

Fig. 6 Dynamic loading protocols for *in-situ* testing at the Port of Longview: (a) schematic of T-Rex and loading of the Silt Array, (b) staged shaking events imposed with increasing dynamic loading amplitudes, (c) blasting time history, and (d) elevation view of the blast array, aligned along a due East-West alignment, showing the relative as-built location of each charge within blast casings (modified after Jana 2021)

Figure 7a illustrates the variation of shear force at the ground surface alongside the associated acceleration (Figure 7b) of the ground surface beneath the T-Rex baseplate during Stage 5 loading. The peak ground surface acceleration reached 2.04*g* during Stage 5. Figures 7c and 7d display the particle velocity and displacement measured using TGP S9 over three orthogonal directions during Stage 5. Following the application of uniaxial shaking in the east-west direction of the Silt Array, the highest particle velocities were recorded in the x-component of the TGP. The peak particle velocity and displacement recorded for these five stages in TGP S9x were 0.066 m/s and 1.16 mm, respectively. Figures 7f and 7h present the measured *in-situ* r_u time history where the computed three-dimensional Cauchy shear strain in three orthogonal directions for the Stage 5 shaking event in Element 1 and Element 2 is shown in Figures 7e and 7g. The T-Rex shaking produced vertically propagating horizontally polarized shear waves that resulted in maximum shear strain in the x-z plane. This is related to the largest particle displacements in the x direction, as seen in Figure 7d. The second highest shear strain is observed in the x-y plane in Element 1 as opposed to the y-z plane in Element 2, because of the center of Element 1 being offset 0.23 m from the front edge of the T-Rex baseplate.

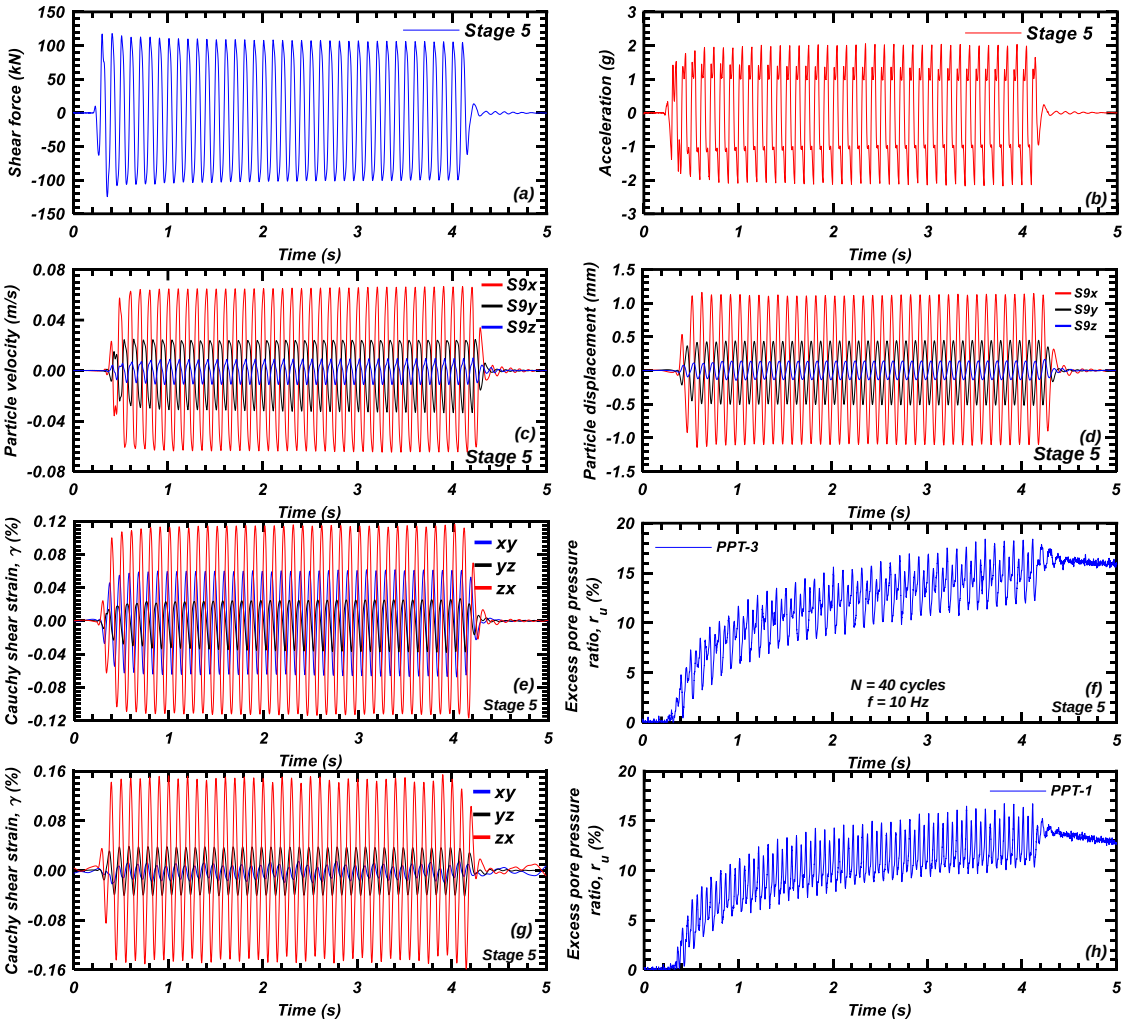

Fig. 7 Results of Stage 5 T-Rex loading: (a) shear force, and (b) recorded acceleration time histories at the ground surface; (c) three-component particle velocity, (d) particle displacement, (e) Cauchy shear strain time histories in Element 1, (f) excess pore pressure ratio in Element 1, (g) Cauchy shear strain in Element 2, (h) and excess pore pressure ratio time histories in Element 2 (modified after Jana et al. 2023)

To establish a relationship between the shear strain and excess pore pressure responses in the silt, the constant-volume, direct simple shear-equivalent shear strain, $\gamma_{DSS,eq}$ was determined for each of the five shaking stages. Because the maximum shear strain, $\gamma_{DSS,max}$, is less than the threshold shear strain, γ_{tp}, to cause residual excess pore pressure, Δu_r in the soil (Dobry et al. 1982), the first stage of loading did not

produce Δu_r, after forty loading cycles, as observed by others(e.g., Mortezaie and Vucetic 2016; Jana and Stuedlein 2021a, 2021b and 2021c). As the shear strain amplitude increased throughout the latter phases of cyclic loading, $r_{u,r}$ increased.

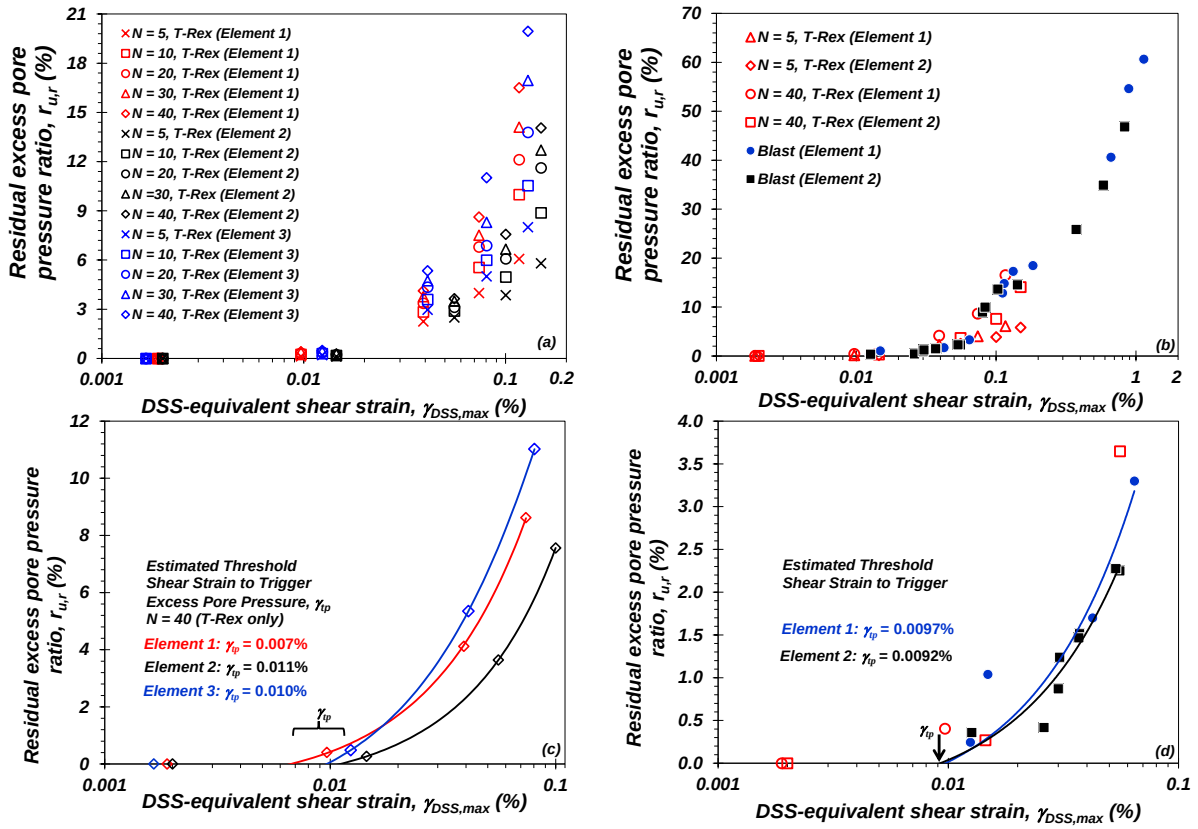

Fig. 8 Relationship of the DSS-equivalent shear strain and excess pore pressure ratio (a) derived from T-Rex loading (b) derived from controlled blasting; relationship of γ_{tp} to trigger $r_{u,r}$ in three elements: (c) derived from T-Rex loading, and (d) derived from controlled blasting (modified after Jana 2021; Jana et al. 2023)

The variation in $r_{u,r}$ with $\gamma_{DSS,max}$ in Elements 1, 2, and 3 for a selected number of cycles, N, and during the five shaking events is shown in 8a. The maximum DSS-equivalent shear strain in Elements 1, 2, and 3 was 0.00089%, 0.002%, and 0.0017, respectively, during Stage 1, and did not induce Δu_r, as γ_{tp} was not exceeded. In Stage 2, the maximum $\gamma_{DSS,max}$ in Elements 1, 2, and 3 was 0.0097%, 0.0145%, and 0.0123%, respectively, corresponding to $r_{u,r}$, N = 40, which equated to 0.40%, 0.27%, and 0.61% in Elements 1, 2, and 3, respectively. The calculated γ_{tp} for Elements 1, 2, and 3 is 0.007%, 0.011%, and 0.010%, respectively. Stage 5 loading resulted in $\gamma_{DSS,max}$ of 0.117%, 0.150%, and 0.129% for Elements 1, 2, and 3, respectively, corresponding to $r_{u,r}$, N = 40 of 16.5%, 14.1%, and 19.9%, respectively.

The instrumented Silt Array was subjected to a controlled blasting event on the day following vibroseis shaking. The variations in excess pore pressure with $\gamma_{DSS,eq}$ are shown in Figures 9a and 9b for each element. It is significant to notice that because Element 1 experienced larger shear strains than Element 2, the excess pore pressure was higher. In contrast to the response anticipated from constant-volume or undrained shearing carried out on laboratory element test specimens, drainage occurred during dynamic shearing as seen in the PPTs. One significant benefit of *in-situ* testing is that it offers a system reaction under actual drainage conditions, which are difficult to replicate in a laboratory setting. The peak shear-induced $r_{u,r}$ recorded in the Silt Array was approximately 61% for Element 1 and 55% for Element 2. The maximum DSS-equivalent shear strains, $\gamma_{DSS,max}$ in Elements 1 and 2 are 1.137% and 0.828%, respectively. Figures 8b and 8d illustrate the correlation between the maximum DSS-equivalent shear strain and $r_{u,r}$ recorded during: (1) T-Rex shaking, and (2) the 30-second blast sequence. The predicted γ_{tp} for Elements 1 and 2 during the controlled blasting event were 0.0097% and 0.0092%, respectively. During the T-Rex shaking, the estimated γ_{tp} for Elements 1, 2, and 3 are 0.007%, 0.011%, and 0.010%, respectively. Although

the magnitude of γ_{tp} derived in these two disparate *in-situ* tests appear to agree well and fall within a narrow range, there are some differences which may be attributed to dynamic pre-straining effects, as described below.

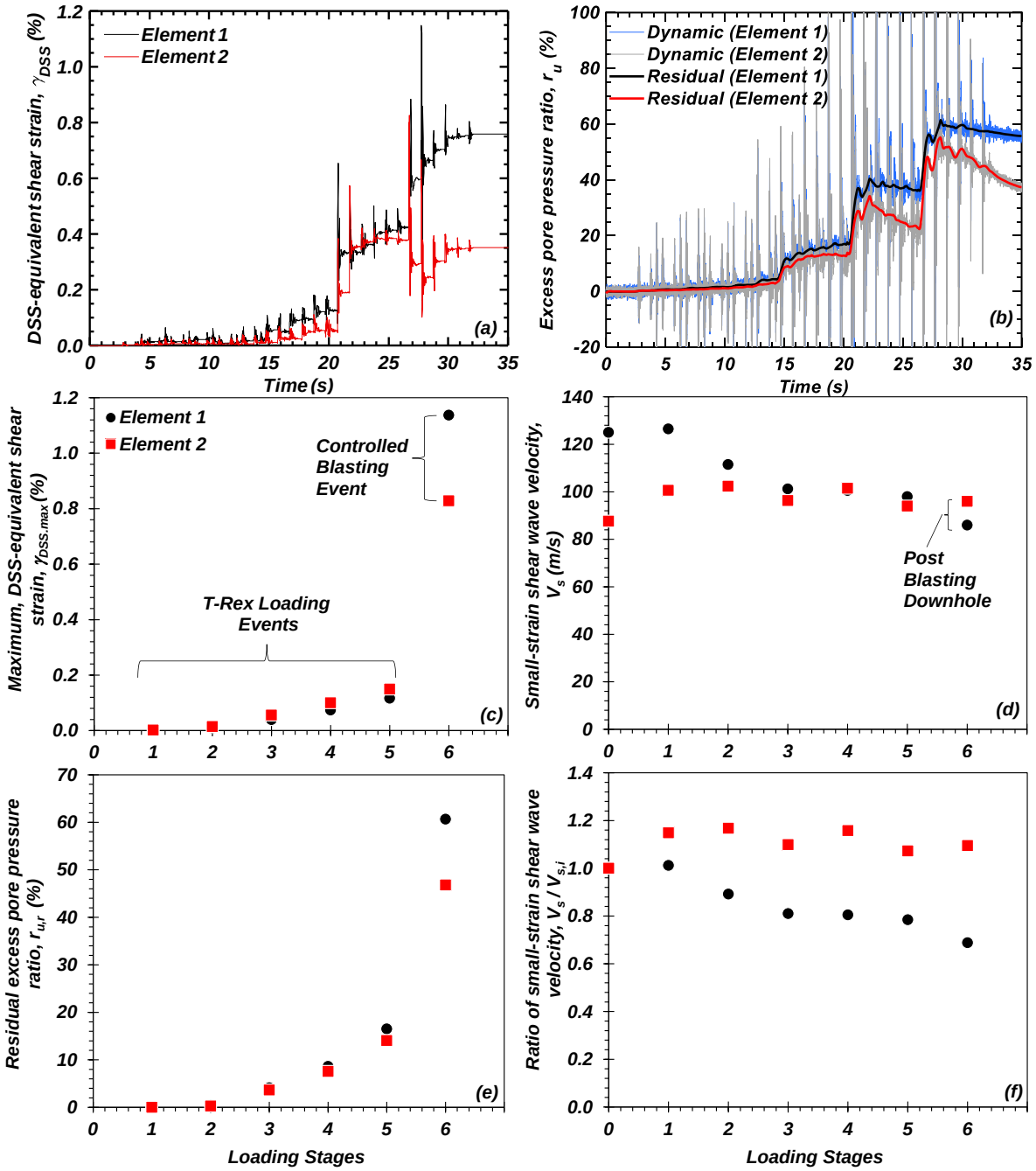

Fig. 9 Staged *in-situ* shaking: (a) DSS-equivalent shear strain time histories and (b) measured dynamic and residual excess pore pressure ratio time histories for Elements 1 (PPT-3) and 2 (PPT-1) during controlled blasting; effect of pre-shaking on dynamic response of silt: (c) shear strain for mild (T-Rex) and large (blast-induced) pre-shakings, and variation of: (d) shear wave velocity, (e) residual excess pore pressure ratio, and (f) ratio of V_s and initial V_s prior to Stage 1 shaking with loading stage (modified after Jana et al. 2023)

To trace the evolution of soil fabric over the multistage dynamic loading of the Silt Array, the average small-strain V_s derived from downhole testing before each stage of T-Rex loading and controlled blasting, and after blasting were measured following dissipation of the excess pore pressures. Prior to T-Rex Stage 1 loading, the average shear wave velocity in Element 1 and Element were 125 m/s and 88 m/s respectively.

Stage 1 T-Rex shaking induced $\gamma_{DSS,max}$ for Element 1 and Element 2 were 0.0019% and 0.002% respectively, which exceeds the nonlinear-inelastic threshold shear strains, γ_{te} (Jana et al. 2023). Relatively small shaking during Stage 1, increases V_s in Element 1 (V_s = 127 m/s) and Element 2 (V_s =101 m/s) through the elimination of local instabilities, enhancing of lateral stresses, and reorganization of soil particles (Finn et al. 1970; El-Sekelly et al. 2017). This finding aligns with the previously established elemental response. Stage 2 shaking exceeded γ_{tp} in both the Elements where $\gamma_{DSS,max}$ for Element 1 and Element 2 were 0.0097% and 0.0145% respectively, resulting some destruction of soil fabric in Element 1 and increase in particle contact in Element 2. This can be viewed through the reduction and increase in V_s following Stage 2 shaking. Following Stage 3 shaking, the V_s in Element 1 reduced from 112 m/s to 101 m/s and, in Element 2, V_s reduced from 102 m/s to 96 m/s. Relatively larger $\gamma_{DSS,max}$ during the Stage 3 shaking caused greater soil fabric destruction which overcome the beneficial effect of dissipation induced soil densification. Stage 4 shaking developed $\gamma_{DSS,max}$ of 0.074% and 0.1% generating $r_{u,r}$ of 9.7% and 8.2% in Element 1 and Element 2 respectively. The dissipation of u_e developed during Stage 4 event could densified the soil deposit resulting increase in V_s and recovery of soil cyclic resistance prior to Stage 5 shaking (Figure 9d). In Element 1 and Element 2, the $r_{u,r}$ values were 18.4% and 16.7%, respectively, as a result of the $\gamma_{DSS,max}$ of 0.12% and 0.15% that were developed during the Stage 5 motion. The beneficial effect of dissipation-induced soil densification was overridden by the larger destruction of soil fabric during Stage 5 shaking. For example, after the excess pore pressure generated during the fifth stage of T-Rex loading had dissipated and the soil had densified, the average small strain V_s in Element 1 reduced from 101 m/s to 98 m/s (Figure 9d). In the case of Element 2, V_s reduced from 102 m/s to 94 m/s following the fifth stage of T-Rex loading. Following 5 stages of T-Rex shaking, the average V_s in Element 1 reduced 31% and the average V_s in Element 2 rose 10% compared to the pre-dynamic event (Figure 9f).

In the controlled blast test program, the soil underwent substantial shear strain of $\gamma_{DSS,max}$ = 1.137% and 0.828% in Elements 1 and 2, respectively, resulting in $r_{u,r}$ of approximately 60.7% and 46.8% in Elements 1 and 2, respectively. The V_s obtained from downhole testing for Elements 1 and 2 were 86 and 96 m/s, respectively, following full dissipation of $r_{u,r}$ in the controlled blasting experiment. The high shear strain in Element 1 resulted in considerable destruction to the soil fabric, which had surpassed the increase in stiffness from densification due to the dissipation of $r_{u,r}$ following the preceding dynamic event (Finn et al. 1970; Oda et al. 2001; Olson et al. 2001; Wahyudi et al. 2016). However, following the controlled blasting, V_s rose in Element 2. While this may be attributed to the marginally reduced $\gamma_{DSS,max}$ and $r_{u,r}$ (El-Sekelly et al. 2016, 2017; Dobry et al. 2019), the drainage in Element 2 (Figure 9b) during controlled blasting certainly enhanced soil resistance. The *in-situ* dynamic testing performed in this study clearly demonstrates the existence of alterations in soil constitutive response attributable to prestraining history, which may elucidate potential implications for evaluating the effects of aftershocks after a mainshock event (Raghunandan et al. 2015; Dobry et al. 2019).

CONTROLLED BLASTING-INDUCED STRAIN HISTORY RESPONSES OF A HIGH PLASTIC SILT DEPOSIT

The previously described *in-situ* dynamic testing experimented showed the effect of strain history of low plasticity silt deposit. A second *in-situ* dynamic test conducted on a medium-to-high plasticity silt deposit serves to reinforce the prior observations in the laboratory and the field. The test site for this second *in-situ* test is situated at the Port of Portland, Portland, Oregon (USA), and is termed Site D as described earlier in the paper. Jana and Stuedlein (2021a, 2022) have provided a detailed description of the pertinent subsurface characteristics; these conditions are briefly discussed below. A layer of recent, alluvial, loose clean sand, about 2 meters thick, lies beneath 5 to 6 m of dredged silty sand fill. Beneath the natural sand layer is an alluvial deposit of medium stiff, clayey silt (MH) with thin lenses of sandy silt (ML) and varying in thickness from 5 to 6 m. A deep deposit of alluvial, medium dense, clean sand (SP) to sand with silt (SP-SM) extends beneath the silt layer and to the depth of the explorations. The response of silt deposit is described herein. The mean PI of the silt deposit is 28, whereas the OCR ranges from 1.6 to 2.2. The soil behavior type index, I_c (Robertson 2009), and corrected cone tip resistance, q_t, range from 2.9 to 3.1 and 0.82 to 1.15 MPa, with averages of 2.99 and 0.95 MPa, respectively, from the depth of 8.89 m to 11.45 m which forms the instrumented Silt Array at this site. The initial average V_s of entire natural silt deposits was approximately 126 m/s determined from *in-situ* downhole experiments (Donaldson 2019).

Three distinct blasting events were carried out at the test site and facilitated exploration of the effect of strain history: the Test Blast Program (TBP), the Deep Blast Program (DBP), and the Shallow Blast Program (SBP). TGPs and PPTs were installed to form the Sand and Silt Arrays, situated at depths of 25 m and 10.2 m, respectively. Figures 10a and 10b presents the locations of the two instrument arrays and the blast casings used to house the explosive charges. The Silt Array was constructed to form two rectangular (2D) elements, designated Elements 1 (with TGPs S3, S4, S6, and S7) and 2 (with TGPs S4, S5, S7, and S8). Two additional, larger finite elements were created using the instruments within the Silt Array in order to assess how element shape affects the computed dynamic response and to make PPT 5 usable (Figure 10b). Specifically, TGPs S8, S4, S3, and S7 and TGPs S7, S5, S4, and S6, were assembled into rhombus-shaped elements to form Elements 3 and 4, respectively.

The purpose of the TBP was to quantify small strain crosshole shear wave velocities in the Silt and Sand Arrays, analyze ground motion attenuation, and assess the data acquisition system. The main aim of the DBP and SBP was to dynamically stimulate the soils within the Sand and Silt Arrays, while the instruments in each array were observed throughout each blast program. Figure 10a illustrates the placement and detonation sequence of the charges for the TBP, DBP, and SBP. In the TBP, charges were situated within a singular casing CX, positioned 30 m west of casing C1 (Jana et al. 2020). Charges were contained in casings C1 to C10 for the DBP, whereas charges were contained in casings C6 to C15 for the SBP. Figures 10c and 10d illustrate the detonation sequences of the two blast programs, each executed with 1-s delays. Charges were detonated in sequence on both sides of the arrays to reverse the polarity of maximal shear strains and shear stresses. These three separate blast programs provide the basis to explore the strain history response of the silt deposit. The average downhole small-strain (linear-elastic) V_s for different TGP pairings was measured in the Silt Array prior to the TBP and SBP.

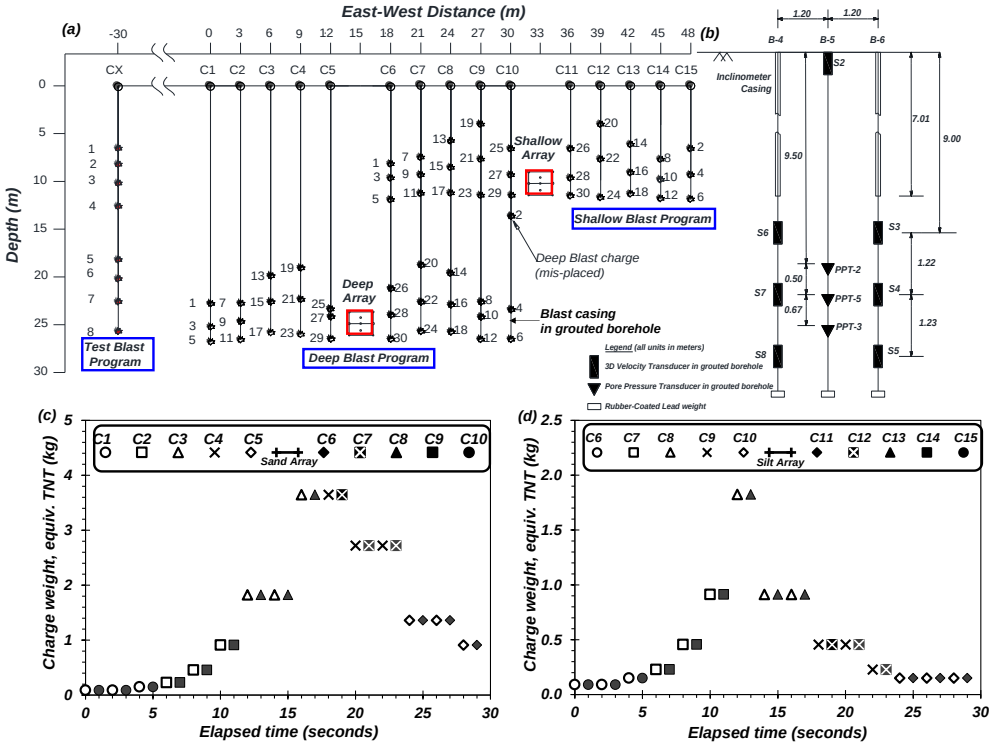

Fig. 10 Elevation view of the blast array, aligned along a due East-West alignment, showing the relative as-built location of each charge within blast casings used in each of the three blast events; (b) elevation view of the as built Silt Array; (c) schematic of the Deep Blast Program indicating charge detonation time history for explosives distributed within blast casings C1 through C10 (d) Detonation time history conducted during the Shallow Blast program within blast casings C6 through C10 and C11 through C15 (modified after Jana 2021; Stuedlein et al. et al. 2023)

Variations in shear strain and excess pore pressure response are shown in Figure 11 for the three blast events. The $r_{u,r}$ measured in Elements 1 and 2 at the end of the TBP were 0.35% and 0.77%, respectively, corresponding to $\gamma_{DSS,max}$ of 0.0118% and 0.0072%. Blast #8 resulted in shear strains in the silt that exceeded γ_{tp}. The γ_{tp} for the virgin silt deposit without past dynamic loading history varies between 0.008 and 0.013%

for the soil inside the two elements. The $\gamma_{DSS,max}$ for the DBP in Elements 1 and 2 were 0.18% and 0.23%, respectively, with corresponding $r_{u,r}$ of 5.39% and 5.69% in Elements 1 and 2, respectively. Owing to the close proximity of the second charge (i.e., DBP Blast #2) to the Silt Array (about 5 m; Figure 10a), the threshold shear strain required to trigger $r_{u,r}$ was surpassed during Blast #2, hindering the accurate assessment of γ_{tp}.

Figure 12 presents the variation of $r_{u,r}$ with $\gamma_{DSS,max}$ for each blast program. The dissipation of the residual excess pore pressure (i.e., $r_{u,r}$ = 5%) and strain history led to a two-fold rise in γ_{tp} during the SBP relative to the initial γ_{tp} observed during the TBP (i.e., 0.008 to 0.016%). The threshold shear strain to trigger $r_{u,r}$ during the SBP ranges from 0.015 to 0.029% (Figure 12b). This observation aligns with the recorded increase in V_s within the Silt Array subsequent to the DBP. Downhole tests undertaken after the DBP were executed to evaluate potential alterations in the soil fabric due to the DBP. Before the test blast program, the average V_s within the instrumented silt deposit was 126 m/s, but prior to the SBP program, the average V_s within the silt deposit was 137 m/s. A mean increase in V_s of 6% is linked to the dissipation of u_e produced during the DBP and the subsequent consolidation (i.e., densification). Silt exposed to low amplitude shear strains exhibits an enhancement in its dynamic shearing resistance, as previously described using element testing and *in-situ* testing at the Port of Longview.

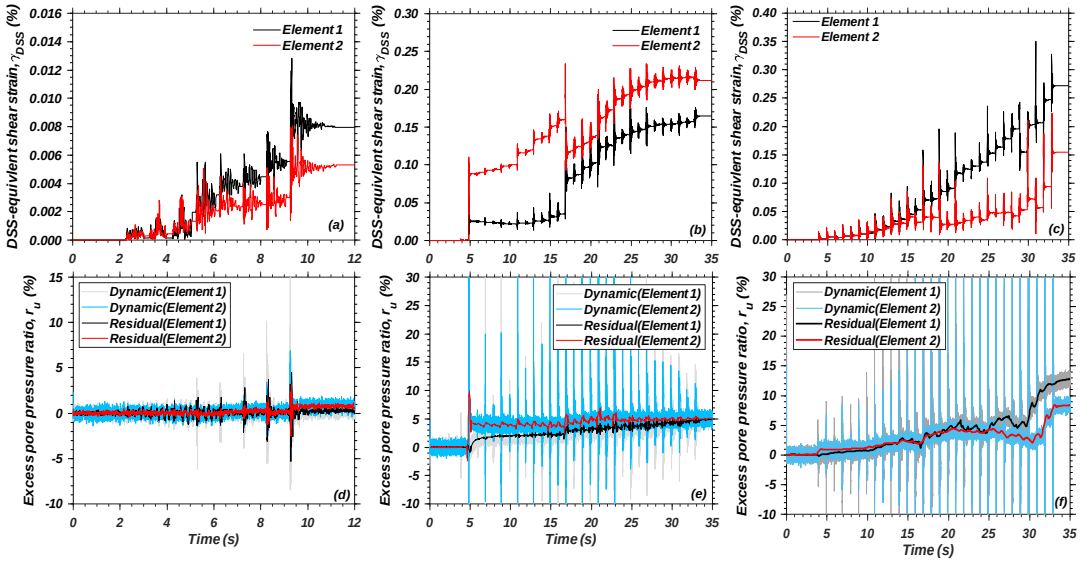

Fig. 11 Dynamic response of the Silt Array at the Port of Portland (Site D) including the variation of the DSS-equivalent shear strain, γ_{DSS} during the: (a) Test Blast Program, (b) Deep Blast Program, and (c) Shallow Blast Program, and the excess pore pressure ratio, r_u, time histories during the: (d) Test Blast Program, (e) Deep Blast Program, and (f) Shallow Blast Program

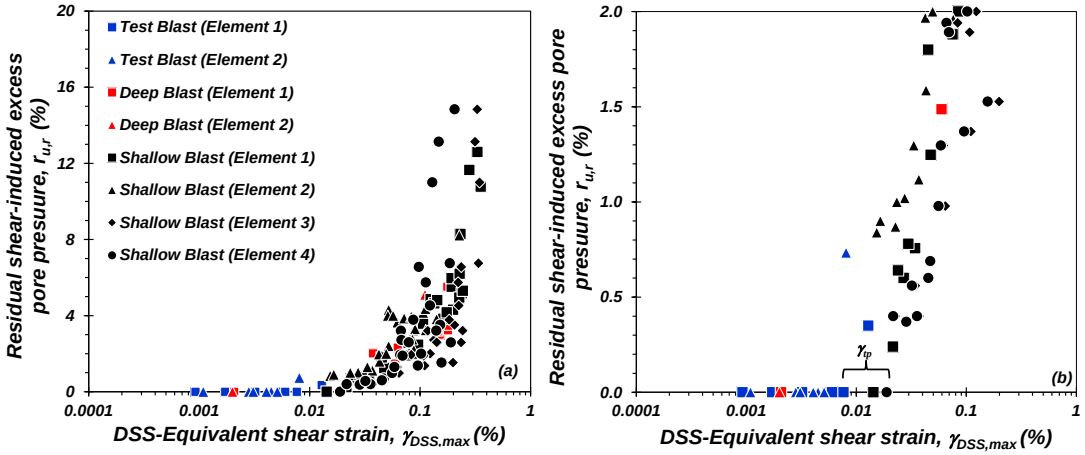

Fig. 12 (a) Variation of excess pore pressure, r_u, and maximum DSS-equivalent shear strain, $\gamma_{DSS,max}$, deduced for the silt array during the TBP, DBP, and SBP; (b) Threshold shear strain to trigger excess pore pressure observed during the blast programs (modified after Jana and Stuedlein 2022)

CONCLUSION

This study presents a comprehensive view into the effect of cyclic and dynamic strain history on the dynamic properties of silts from element and *in-situ* tests. The element tests were performed using a cyclic direct simple shear apparatus with capability of small strain shear wave velocity measurements. The element tests indicate that the smaller pre-shaking did not significantly alter the density of the specimens; however, it may enhance soil fabric by eliminating local instabilities, increasing lateral pressure coefficients, and modifying the arrangement of soil particles, as suggested by the increasing trend of V_s. In most instances, specimens subjected to constant cyclic stress ratio during various shearing and reconsolidation phases demonstrated a net enhancement in cyclic resistance, primarily due to increased dilation from post-cyclic densification, reorganization of soil particles leading to improved interlocking mechanisms, and a probable rise in lateral stresses. The assessment of cyclic resistance, based in several failure strain criteria, may yield markedly different outcomes during succeeding loading phases. The magnitude of maximum shear strain generated during initial loading phases can enhance or diminish the cyclic resistance in later stages.

Field research indicates that soil deposits subjected to small shear strain history exhibit an increase in stiffness, corroborated by alterations in the threshold shear strain required to initiate excess pore pressure generation, γ_{tp}, in the soil. It has been noted that γ_{tp} increases with the stiffness-driven behavior of the micromechanical model described by Dobry and associates (e.g., Dobry et al. 1982). It is also observed that large shear strains caused destruction in soil fabric leading to lower shear stiffness as observed from the reduction in shear wave velocity. The *in-situ* dynamic tests distinctly reveal changes in the nonlinear-inelastic soil constitutive response attributable to strain history and differing drainage boundary conditions.

ACKNOWLEDGMENTS

We are grateful to Professor Kenneth H. Stokoe, Professor Brady R. Cox, Dr. Benchen Zhang, and Dr. Zhongze (Steve) Xu for their productive discussions and collaboration at the Port of Longview site. The National Science Foundation (Grant CMMI 1663654) provided the authors with support during the course of the experiments conducted at the Port of Longview. The authors are also grateful for the sponsorship of this work by the Cascadia Lifelines Program (CLiP) and its members. Thanks are due to Anne Trehu, James Batti, Aleyna Donaldson, and Erick Moreno-Rangel for their participation in discussions and/or assistance with various aspects of study at Port of Portland. We extend special gratitude to the Port of Portland and Port Engineer Tom Wharton, P.E., for the studies conducted at the Port of Portland. Any opinions, findings, and conclusions conveyed are solely those of the authors and do not necessarily represent the perspectives of the sponsors.

REFERENCES

1. Cubrinovski, M., Bradley, B., Wotherspoon, L., Green, R., Braym J., Woodm C., Pender, M., Allen, J., Bradshaw, A., Rix, G. and Taylor, M. (2011). "Geotechnical Aspects of the 22 February 2011 Christchurch Earthquake", *Bulletin of the New Zealand Society for Earthquake Engineering*, Vol. 44, No. 4, pp. 205-226.
2. Dadashiserej, A. (2022). "Laboratory Investigation of the Cyclic Response of Transitional Soils: Bridging Element-Scale and *In-situ* Responses", *PhD Thesis, Oregon State University*.
3. Dadashiserej, A., Jana, A., Ortiz, S.C., Walters, J.J., Stuedlein, A.W. and Evans, T.M. (2022). "Monotonic, Cyclic, and Post-Cyclic Response of Willamette River silt at the Van Buren Bridge", *In Geo-Congress*, pp. 431-443.
4. Dadashiserej, A., Jana, A., Stuedlein, A.W. and Evans, T.M. (2022). "Effect of Strain History on the Monotonic and Cyclic Response of Natural and Reconstituted Silts", *Soil Dynamics and Earthquake Engineering*, Vol. 160, pp. 107329.
5. Dadashiserej, A., Janam A., Xu, Z., Stuedlein, A.W., Evans, T.M., Stokoe, K.H. and Cox, B.R. (2024). "Dynamic Response of a Low Plasticity Silt Deposit: Comparison of *In-situ* and Laboratory Responses", *Canadian Geotechnical Journal*, Vol. 61, pp. 1399–1417.

6. Dobry, R. and Abdoun, T. (2015). "Cyclic Shear Strain Needed for Liquefaction Triggering and Assessment of Overburden Pressure Factor Kσ", *J. of Geotech. Geoenv. Eng.*, Vol. 141, No. 11, pp. 04015047.
7. Dobry, R., Ladd, R.S., Yokel, F.Y., Chung, R.M. and Powell, D. (1982). "Prediction of Pore Water Pressure Buildup and Liquefaction of Sands During Earthquakes by the Cyclic Strain Method", *Gaithersburg, MD: National Bureau of Standards*, Vol. 138.
8. Dobry, R., Thevanayagam, S., El-Sekelly, W., Abdoun, T. and Huang, Q. (2019). "Large-Scale Modeling of Preshaking Effect on Liquefaction Resistance, Shear Wave Velocity, and CPT Tip Resistance of Clean Sand", *Journal of Geotechnical and Geoenvironmental Engineering*, Vol. 145, No. 10, pp. 04019065.
9. Donaldson, A.M. (2019). "Characterization of the Small-Strain Stiffness of Soils at an *In-situ* Liquefaction Test Site", *MS Thesis, Oregon State University*, pp. 287.
10. El-Sekelly, W., Dobry, R., Abdoun, T. and Steidl, J.H. (2016). "Centrifuge Modeling of the Effect of Preshaking on the Liquefaction Resistance of Silty Sand Deposits", *Journal of Geotechnical and Geoenvironmental Engineering*, Vol. 142, No. 6, pp. 04016012.
11. El-Sekelly, W., Dobry, R., Abdoun, T. and Steidl, J.H. (2017). "Two Case Histories Demonstrating the Effect of Past Earthquakes on Liquefaction Resistance of Silty Sand", *Journal of Geotechnical and Geoenvironmental Engineering*, Vol. 143, No. 6, pp. 04017009.
12. Finn, W.L., Bransby, P.L. and Pickering, D.J. (1970). "Effect of Strain History on Liquefaction of Sand", *Journal of Soil Mechanics & Foundations Div.*, Vol. 96, No. 6.
13. Hayati, H. and Andrus, R.D. (2009). "Updated Liquefaction Resistance Correction Factors for Aged Sands", *Journal of Geotechnical and Geoenvironmental Engineering*, Vol. 135, No. 11, pp. 1683-1692.
14. Holzer, T.L. and Youd, T.L. (2007). "Liquefaction, Ground Oscillation, and Soil Deformation at the Wildlife Array, California", *Bulletin of the Seismological Society of America*, Vol. 97, No. 3, pp. 961-976.
15. Hsu, C.C. and Vucetic, M. (2006). "Threshold Shear Strain for Cyclic Pore-Water Pressure in Cohesive Soils", *Journal of Geotechnical and Geoenvironmental Engineering*, Vol. 132, No. 10, pp. 1325-1335.
16. Idriss, I.M. and Boulanger, R.W. (2008). "Soil Liquefaction during Earthquakes", *Earthquake Engineering Research Institute*.
17. Ishihara, K. and Okada, S. (1978). "Effects of stress history on cyclic behavior of sand", *Soils and Foundations*, Vol. 18, No. 4, pp. 31-45.
18. Jana, A. (2021). "Use of Controlled Blasting to Quantify the Dynamic, *In-Situ*, Nonlinear Inelastic Response of Soils", *PhD Thesis, Oregon State University*.
19. Jana, A. and Stuedlein, A.W. (2021a). "Monotonic, Cyclic and Post-Cyclic Response of an Alluvial Plastic Silt Deposit", *Journal of Geotechnical and Geoenvironmental Engineering*, Vol. 147, No. 3, pp. 04020174.
20. Jana, A. and Stuedlein, A.W. (2021b). "Dynamic, In-situ, Nonlinear-Inelastic Response of a Deep, Medium Dense Sand Deposit", *Journal of Geotechnical and Geoenvironmental Engineering*, Vol. 147, No. 6, pp. 04021039.
21. Jana, A. and Stuedlein, A.W. (2022). "Dynamic, *In-situ*, Nonlinear-Inelastic Response and Post-Cyclic Strength of a Plastic Silt Deposit", *Canadian Geotechnical Journal*, Vol. 59, No. 1, pp. 111-128.
22. Jana, A., Dadashiserej, A., Zhangm B., Stuedleinm A.W., Matthew, Evans T., Stokoe, K.H. and Cox, B.R. (2023). "Multi-directional VibroSeis Mobile Shaking and Controlled Blasting to Determine the In-situ Dynamic Response of a Low Plasticity Silt Deposit", *Journal of Geotechnical and Geoenvironmental Engineering (ASCE)*, Vol. 149, No. 3.
23. Jana, A., Donaldson, A.M., Stuedlein, A.W. and Evans, T.M. (2021). "Deep, In-situ Nonlinear Dynamic Testing of Soil with Controlled Blasting: Instrumentation, Calibration, and Example Application to a Plastic Silt Deposit", *Geotechnical Testing Journal*, Vol. 44, No. 5, pp. GTJ20190426.
24. Krage, C.P., Price, A.B., Lukas, W.G., DeJong, J.T., DeGroot, D.J. and Boulanger, R.W. (2020). "Slurry Deposition Method of Low-Plasticity Intermediate Soils for Laboratory Element Testing", *Geotechnical Testing Journal*, Vol. 43, No. 5.

25. Kuribayashi, E. and Tatsuoka, F. (1975). "Brief Review of Liquefaction during Earthquakes in Japan", *Soils and Foundations,* Vol. 15, No. 4, pp. 81-92.
26. Lee, K.L. and Albaisa, A. (1974). "Earthquake Induced Settlements in Saturated Sands", *Journal of Geotechnical and Geoenvironmental Engineering,* Vol. 100, pp. 10496.
27. Mortezaie, A. and Vucetic, M. (2016). "Threshold Shear Strains for Cyclic Degradation and Cyclic Pore Water Pressure Generation in Two Clays", *J. of Geotech. Geoenv. Eng.,* Vol. 142, No. 5, pp. 04016007.
28. Oda, M., Kawamoto, K., Suzuki, K., Fujimori, H. and Sato, M. (2001). "Microstructural Interpretation on Reliquefaction of Saturated Granular Soils under Cyclic Loading", *Journal of Geotechnical and Geoenvironmental Engineering,* Vol. 127, No. 5, pp. 416-423.
29. Olson, S.M., Obermeier, S.F. and Stark, T.D. (2001). "Interpretation of Penetration Resistance for Back-Analysis at Sites of Previous Liquefaction", *Seismological Research Letters,* Vol. 72, No. 1, pp. 46-59.
30. Price, A.B., DeJong, J.T. and Boulanger, R.W. (2017). "Cyclic Loading Response of silt with Multiple Loading Events", *Journal of Geotechnical and Geoenvironmental Engineering,* Vol. 143, No. 10, pp. 04017080.
31. Raghunandan, M., Liel, A.B. and Luco, N. (2015). "Aftershock Collapse Vulnerability Assessment of Reinforced Concrete Frame Structures", *Earthquake Engineering & Structural Dynamics,* Vol. 44, No. 3, pp. 419-439.
32. Robertson, P. (2009). "Interpretation of Cone Penetration Tests a Unified Approach", *Can. Geotech. J.,* Vol. 46, No. 11, pp. 1337–1355.
33. Sanin, M.V. (2005). "Cyclic Shear Loading Response of Fraser River Delta Silt", *Doctoral dissertation, University of British Columbia*.
34. Soysa, A. and Wijewickreme, D. (2017). "Comparison of Cyclic Shear Response of Three Natural Fine-Grained Soils Having Different Plasticity", *Proc., Proc. of the 16th World Conference on Earthquake Engineering, Santiago, Chile, No. 0550*.
35. Soysa, A. and Wijewickreme, D. (2019). "Repeated Cyclic Shear Loading Response of Reconstituted Fraser River Silt", *Proc., Proceedings of the 7th International Conference on Earthquake Geotechnical Engineering, Rome, Italy*.
36. Stokoe, K., Cox, B., Clayton, P. and Menq, F. (2017). "NHERI@ UTEXAS Experimental Facility: Large-Scale Mobile Shakers for Natural-Hazards Field Studies", *In 16th World Conference on Earthquake Engineering,* pp. 9-13.
37. Stuedlein, A.W., Dadashiserej, A., Jana, A. and Evans, T.M. (2022). "Liquefaction Susceptibility and Cyclic Response of Intact Nonplastic and Plastic Silts", *Journal of Geotechnical and Geoenvironmental Engineering,* Vol. 149, No. 1, pp. 04022125.
38. Stuedlein, A.W., Jana, A., Dadashiserej, A. and Yang, X. (2023). "On the In-situ Cyclic Resistance of Natural Sand and Silt Deposits", *Journal of Geotechnical and Geoenvironmental Engineering (ASCE),* Vol. 149, No. 4, pp. 04023015.
39. Van Ballegooy, S., Malan, P., Lacrosse, V., Jacka, M.E., Cubrinovski, M., Bray, J.D., O'Rourke, T.D., Crawford, S.A. and Cowan, H. (2014). "Assessment of Liquefaction-Induced Land Damage for Residential Christchurch", *Earthquake Spectra,* Vol. 30, No. 1, pp. 31-55.
40. Wahyudi, S., Koseki, J., Sato, T. and Chiaro, G. (2016). "Multiple-Liquefaction Behavior of Sand in Cyclic Simple Stacked-Ring Shear Tests", *International Journal of Geomechanics,* Vol. 16, No. 5, pp. C4015001.
41. Wijewickreme, D. and Soysa, A. (2016). "Stress–Strain Pattern–Based Criterion to Assess Cyclic Shear Resistance of Soil from Laboratory Element Tests", *Canadian Geotechnical Journal,* Vol. 53, No. 9, pp. 1460-1473.
42. Wijewickreme, D., Soysa, A. and Verma, P. (2019). "Response of Natural Fine-Grained Soils for Seismic Design Practice: A Collection of Research Findings from British Columbia, Canada", *Soil Dynamics and Earthquake Engineering,* Vol. 124, pp. 280-296.
43. Youd, T.L. and Bennett, M.J. (1983). "Liquefaction Sites, Imperial Valley, California", *Journal of Geotechnical Engineering,* Vol. 109, No. 3, pp. 440-457.